

ARTICLE OPEN

Room-Temperature Graphene-Nanoribbon Tunneling Field-Effect Transistors

Wan Sik Hwang^{1,2,3*}, Pei Zhao², Sung Geun Kim⁴, Rusen Yan¹, Gerhard Klimeck⁴, Alan Seabaugh², Susan K. Fullerton-Shirey^{2,5}, Huili Grace Xing^{1,2,6} and Debdeep Jena^{1,2,6*}

Controlled, tunable, and reversible negative-differential resistance (NDR) is observed in lithographically defined, atomically thin semiconducting graphene nanoribbon (GNR)-gated Esaki diode transistors at room temperature. Sub-10 nm-wide GNRs patterned by electron-beam lithography exhibit semiconducting energy bandgaps of ~ 0.2 eV extracted by electrical conductance spectroscopy measurements, indicating an atomically thin realization of the electronic properties of conventional 3D narrow-bandgap semiconductors such as InSb. A p - n junction is then formed in the GNR channel by electrostatic doping using graphene side gates, boosted by ions in a solid polymer electrolyte. Transistor characteristics of this gated GNR p - n junction exhibit reproducible and reversible NDR due to interband tunneling of carriers. All essential experimentally observed features are explained by an analytical model and are corroborated by a numerical atomistic simulation. The observation of tunable NDR in GNRs is conclusive proof of the existence of a lithographically defined bandgap and the thinnest possible realization of an Esaki diode. It paves the way for the thinnest scalable manifestation of low-power tunneling field-effect transistors (TFETs).

npj 2D Materials and Applications (2019)3:43; <https://doi.org/10.1038/s41699-019-0127-1>

INTRODUCTION

The single-atom thickness of a two-dimensional (2D) sheet of graphene represents the ultimate limit of how thin one can make an electronically active material.^{1–3} At present, there is no known way to scale a three-dimensional (3D) semiconductor to such a thickness. Structurally, this is not possible, because the chemical bonds are inherently 3D and a unit cell of the crystal cannot be completed in 2D.⁴ Electronically, as a conventional 3D-crystal semiconductor is made thinner to approach the single-atom thickness limit, quantum confinement of electron states increases the energy bandgap.⁴ As graphene has a two-atom basis, the on-site energies for an electron for the A- and B-atom sites are identical (both are carbon atoms) and the energy bandgap is zero. The zero gap prevents an appreciable modulation of the electronic conductivity upon sweeping the Fermi level through the Dirac point, preventing the realization of traditional Boolean On/Off electronic transistor switches. Nevertheless, several devices that exploit the uniqueness of the bandstructure and the density of states of graphene have been theoretically envisioned and experimentally demonstrated.^{5,6}

How can the bandgap be opened in an atomically thin material? One way is to break the chemical symmetry of graphene. This is achieved, e.g., in hexagonal boron nitride (hBN), where B and N are the nearest-neighbor atoms that straddle carbon in the same row of the periodic table. hBN is the compound-semiconductor analog of graphene, where the broken chemical symmetry due to the different on-site energies for the basis atoms opens a bandgap ~ 5 eV.^{7,8} Because of the large energy gap and chemical inertness, hBN has been used as an insulating barrier for atomically flat and clean van-der-Waals heterointerfaces.^{9–11} It is possible that in the future similar atomically thin compound materials with bandgaps smaller than hBN will be discovered. A number of gapped

semiconductors with broken chemical symmetry exist for thicknesses of tri-atomic layers and beyond, such as the three-atom-thick MoS₂ family, the four-atom-thick GaSe family, etc.^{12–14} However, as the electrostatic scaling length of a transistor channel goes as $\lambda = \sqrt{\frac{\epsilon_s}{\epsilon_{ox}} t_s t_{ox}}$ where λ is the electrostatic scaling length, ϵ_s and ϵ_{ox} are the permittivities of semiconductor and gate oxide, and t_s and t_{ox} are the thicknesses of the semiconductor channel and the gate oxide, respectively; the thickness of the channel itself will soon become the limiting factor, for which a one-atom-thick material trumps all others.

If chemical symmetry were to be preserved, other symmetries need to be broken to open gaps, e.g., by starting from zero-gap bilayer graphene (no more an atomically thin material) and applying a vertical electric field opens a bandgap.^{15,16} Alternately, a gap can be opened by letting the atomic sites pucker out of plane. For example, this geometric symmetry breaking opens bandgaps in phosphorene.^{17,18} Carbon nanotubes (CNTs) allow a way to break the cylindrical symmetry by requiring the electron wavefunction to satisfy periodic boundary conditions around the circumference. Depending on the chiral wrapping (armchair vs. zig-zag) and the radius, the density of electronic states of carbon nanotubes change from metallic to semiconducting.¹⁹ Semiconducting nanotubes have been used to demonstrate highly scaled field-effect transistors (FETs) that help fight short-channel degradation because of exceptional electrostatic control in small geometries.²⁰ Nanotubes remain highly attractive for electronic switches. Significant progress has been made in the separation of semiconducting and metallic tubes.²¹ Techniques are being developed to assemble them in specified locations. A lack of precise control over the diameter and chirality results in a lack of control over the bandgap, which is required to make identical electronic switches in large numbers. For large-area applications

¹Department of Electrical and Computer Engineering, Cornell University, Ithaca, NY 14853, USA. ²Department of Electrical Engineering, University of Notre Dame, Notre Dame, IN 46556, USA. ³Department of Materials Engineering, Korea Aerospace University, Goyang 10540, Korea. ⁴Department of Electrical and Computer Engineering, Purdue University, West Lafayette, IN 47906, USA. ⁵Department of Chemical and Petroleum Engineering, University of Pittsburgh, Pittsburgh, PA 15213, USA. ⁶Department of Materials Science and Engineering, Cornell University, Ithaca, NY 14853, USA. *email: whwang@kau.ac.kr; djena@cornell.edu

where high-performance is not necessary, (CNT) FETs are making progress.²²

Transistor on/off switching characteristics that beat the fundamental room-temperature “Boltzmann” limit of $(kT/q)\ln(10) \sim 60$ mV/decade were observed in carbon nanotube channel transistors.²³ This observation spurred significant recent interest in an energy-efficient tunneling FETs (TFETs) in several 3D material systems.²⁴ However, as the transistor size is scaled, the energy bandgaps of 3D tunneling junctions increase due to quantum confinement,⁴ exponentially reducing the on-state tunneling current. This necessitates the use of intrinsically reduced dimensional 2D or one-dimensional (1D) semiconductor materials for scaled TFETs. In an in-plane 2D semiconductor tunnel junction, electrons that are incident on the potential barrier at non-90° angles have their tunneling probabilities lowered exponentially;^{25,26} this severe filtering rule reduces the tunneling efficiency, suggesting 1D channels as the most energy-efficient for nanoscale TFETs. This is borne out in benchmarking efforts by the semiconductor industry; a GNR-TFET can outperform all currently conceived low-power switches based on charge, spin, excitons, and negative capacitance under the energy-delay product metric.²⁷

Semiconducting graphene nanoribbons (GNRs) with perfectly controlled edges are the most desirable channel materials for TFETs,^{26–29} although not without their own slew of fabrication challenges. Although CNTs are perfectly cylindrical, GNRs lay flat on a substrate and have broken bonds at the edge. This apparent problem may well become a defining feature. It has proven chemically difficult to dope a CNT by the substitution of donor or acceptor atoms, because there are no sites available for covalent bonding. This opportunity is available in GNRs. The possibility of large-area 2D lithographic patterning, the ability to grow large-area graphene,³⁰ the excellent heat dissipation on account of laying flat on the substrate,³¹ and all the other reasons described above make GNR TFETs a difficult, yet desirable challenge. In this work, we present the experimental realization of a room-temperature GNR-TFET. Although the techniques used here, and the performance, are far from what is desired of a high-performance TFET, our demonstration proves conclusively that the dream of a lithographically defined atomically thin 1D TFET platform is not just conceptually sound, it is experimentally feasible. The theoretical analysis of experiments helps identify the research directions that can take this initial demonstration to a truly attractive low-power sub-Boltzmann switch.

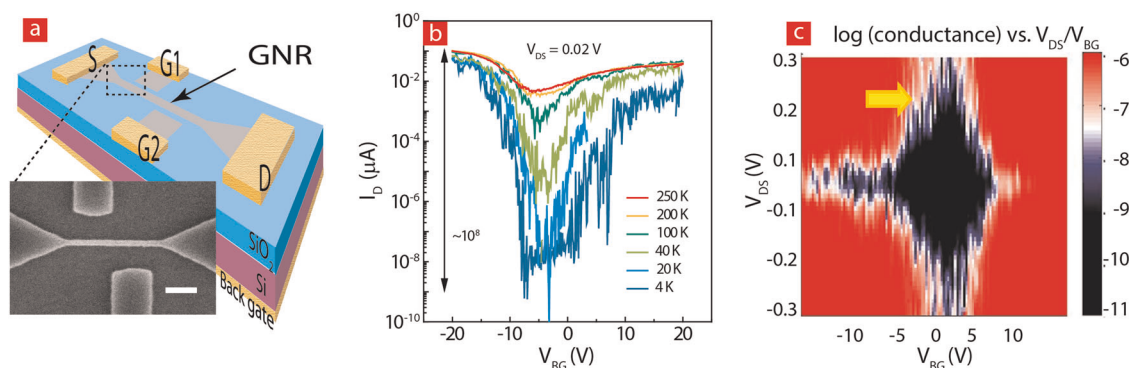


Fig. 1 Graphene nanoribbon (GNR) tunneling field-effect transistors (TFETs). **a** Schematic of back-gated GNR-TFETs with two side gates that form the p - n junction through electrostatic doping. The insets represent corresponding SEM images of the GNR-TFET. The GNR channel and the graphene side gates are covered by hydrogen silsesquioxane (HSQ). The scale bar is 50 nm. **b** Transfer characteristics of a back-gated CVD GNR-FET with GNR of sub-10 nm width. **c** Differential conductance map of the GNR as a function of V_{DS} and V_{BG} at 4 K showing an energy bandgap. The arrow shows the gap

RESULTS AND DISCUSSION

In a recent work,^{32,33} we experimentally showed that lithographically defined atomically thin, ~ 10 nm-wide GNR-FETs (not TFETs) could mimic the electronic behavior of InSb nanowire FETs³⁴ in switching, showing the opening of an energy bandgap of the order of ~ 0.2 eV (the bandgap of InSb is ~ 0.17 eV). In Fig. 1a, we show an image of a similarly fabricated sub-10 nm back-gated GNR-FET, but now with two additional side gates to enable the Esaki diode formation, and realization of a GNR TFET. The entire graphene region, the long GNR channel, and the side gates are patterned from a monolayer chemical vapor deposition (CVD)-grown graphene using electron-beam lithography (Supplementary Fig. S1). The source and drain contacts to the GNR are made to zero-gap wide 2D graphene regions.^{32,33} Figure 1b shows the measured temperature-dependent transfer characteristics and Fig. 1c shows the conductance spectrum measured at 4 K without side-gate bias for the “control” GNR-FET. The conductance modulation and its temperature dependence indicates the opening of an energy bandgap of ~ 0.2 eV for the GNR channel. The measured data and its temperature dependence looks remarkably similar to that of an InSb nanowire FET of gap ~ 0.17 eV.³⁴ However, as the GNRs are lithographically defined, they remain atomically thin as opposed to carbon nanotubes and InSb nanowires, and can be produced in large and reproducible quantities because of significant advances in lithography. For example, the widths of fins in current Si FinFETs are well below 10 nm³⁵ and such processing tools can be brought to action to mass produce tightly controlled narrow GNRs in the future if there is promise in their behavior.

We then test the effect of side gates to introduce a p - n junction in the GNR channel (Supplementary Fig. S2). Although techniques to chemically dope GNRs have been reported,^{36–40} they have yet to provide the degree of control necessary for the demonstration of the TFET action. We have therefore chosen a solid polymer electrolyte gate in this work to enable the side gates to dope the GNR channel locally (Supplementary Fig. S2). Although both solid polymer electrolytes⁴¹ and ionic liquids⁴² are frequently used to gate organic and inorganic FETs, we choose a solid polymer electrolyte, because it is solid state and has a low gate to source leakage current.⁴³ Furthermore, the electrolytes polyethylene oxide (PEO) and LiClO_4 s have been used previously to induce charge carrier densities in 2D graphene greater than $n \sim 10^{13} \text{ cm}^{-2}$.⁴⁴ Figure 2a schematically shows how the polarity of the gate sets the channel doping: when a negative voltage is applied to side-gate 2, the positive Li ions are attracted to the gate pad and the negative ClO_4 ions to the GNR channel. This causes the

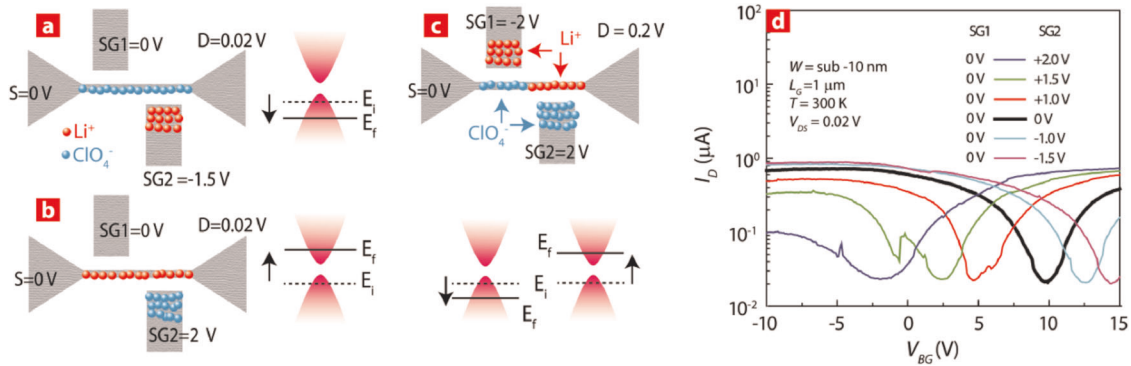


Fig. 2 Electrostatic doping of GNRs using electrolyte gating. Schematic view of electrostatic control of GNRs forming **a** *p*-type, **b** *n*-type, and **c**, *p*-*n* junction in the channel using positive (Li^+) and negative (ClO_4^-) ions in polyethylene oxide (PEO). There are equal numbers of positive and negative ions within each conditions **a–c**, to satisfy the requirements of electro-neutrality. **d** Transfer characteristics of back-gated CVD GNR-FETs demonstrating how the carrier density and carrier type can be modulated using side gates. In contrast to the charge-neutrality point of the GNR-FET in Fig. 1b around -5 V, that of the GNR-FET coated with the solid polymer electrolyte shifted to 10 V, showing that the solid polymer electrolyte dopes the channel even in the absence of a gate voltage

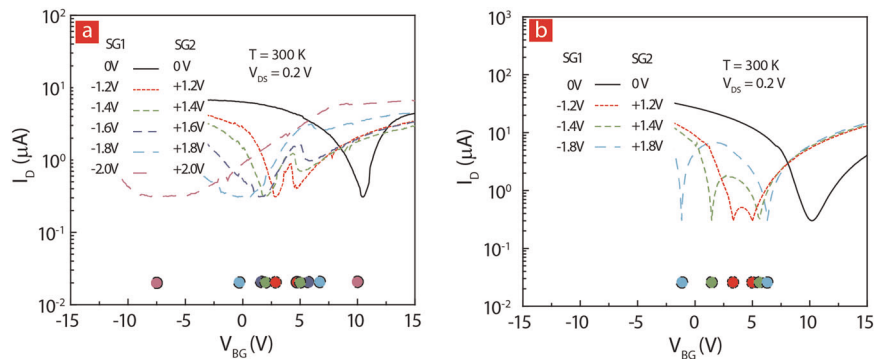


Fig. 3 Formation of *p*-*n* junction in the GNRs via electrostatic control using a side gate and a polymer electrolyte. Drain current, I_D , vs. back-gated, V_{BG} at different voltages at SG1 and SG2. **a** Experimental results. **b** Analytical modeling results. The dots on the x axes indicate the V_{BG} where the minima in the transfer characteristics occur. The position of the dots in the y axes are guides to the eye to compare experiments and theory

GNR channel to be doped *p*-type. Then a higher positive back-gate voltage should be necessary to move the Fermi level to its charge-neutrality point. The experimental positive shift in the measured room-temperature transfer curve shown in Fig. 2d. By varying the side-gate voltage, the measured drain current in Fig. 2d shows that the GNR channel can be doped *n*- or *p*-type by a single side gate. Figure 2c schematically shows that if voltages of opposite polarity are applied to the two side gates, a *p*-*n* junction should form in the GNR channel.

Figure 3a shows the transfer characteristics of the device when the side gates are biased with opposite polarity. Two charge-neutrality points appear in the experimentally measured transfer characteristics, proving the formation of a *p*-*n* junction in the GNR channel.³⁶ Although the measurement was conducted at room temperature, any possibility of Joule heating was ruled out during the operation, based on the low drain voltage of 0.2 V and excellent heat dissipation of graphene, there might be a very little chance for the heat to affect the device performance. The voltage difference between two current minima increases with the strength of the side-gate bias, as indicated by the circles in the figure. This is simply because the side gates are far more effective in doping the GNR channel than the back gate. The use of ions, their unfettered access to the GNR channel, and their inability to participate in the electron current transport are responsible for this significant enhancement. Figure 3b shows the calculated transfer characteristics of the GNR-TFET using a simple analytical model.³² The simple model uses thermionic emission and

tunneling currents in the channel, appropriately gated with the device capacitances, and captures the entire region of operation of the experimentally measured transfer curve, including the splitting and movement of the charge-neutrality points (see Supplementary Section 3 and Fig. S3). This agreement also indicates the band-like transport in the GNR channel (as opposed to hopping) and the successful realization of a gated GNR *p*-*n* junction. The comparison between experiment and model showed that the charge-neutrality points (Fig. 3a) are changing exponentially, while the points (Fig. 3b) are changing linearly. The difference could possibly be attributed to the difference in ion mobility between Li^+ and ClO_4^- . Whereas in the modeling work, the Li^+ and ClO_4^- ions respond at the same rate to the same potential, in reality the movement is likely to be different because of differences in ion size, mobility, and changes in local dynamics with changing ion concentration. In addition, as shown in this comparison between experiment and model, the on-current density of $6 \mu\text{A}/10 \text{ nm}$ at a supply voltage of 0.2 V was experimentally obtained, while that of $40 \mu\text{A}/10 \text{ nm}$ at a supply voltage of 0.2 V was extracted by the model. The degraded on-current density of the GNR-FET compared with the modeled value was presumably due to the imperfect characteristic of the formed GNR such as edge disorder and defects. This difference of around ten times between experiment and model can also be found in ref.²⁸ The currents in Fig. 3 are at a fixed drain bias of 0.2 V; the proof of tunneling is in the $I_d - V_{ds}$ output characteristics of the GNR TFETs shown in Fig. 4.

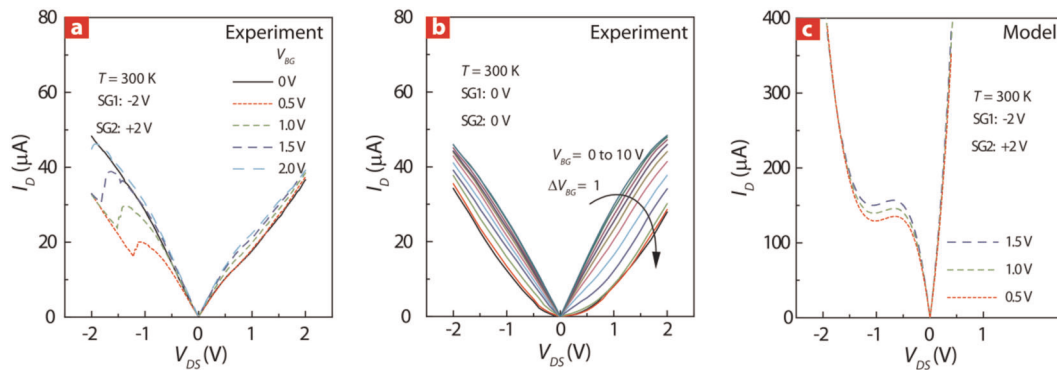


Fig. 4 Output characteristics showing negative-differential resistance (NDR) for electrolyte-gated GNR-TFETs. Absolute value of the drain current, I_D , vs. drain voltage, V_{DS} . **a** NDR-FET behavior at $V_{DS} < 0$ resulting from the tunneling current through the p - n junction formed by additional side gate and typical FET behavior at $V_{DS} > 0$. **b** Normal FET behavior in p -type channel. **c** Analytical modeling of NDR-FET behavior

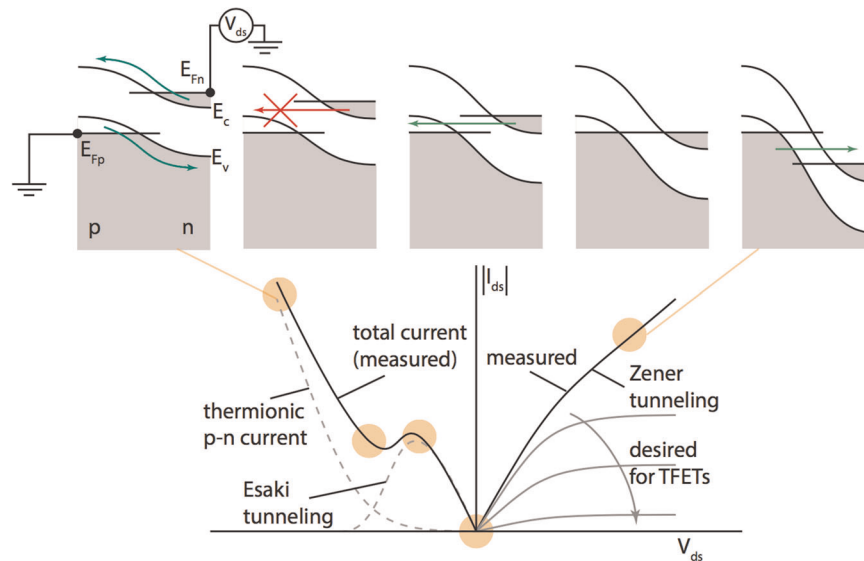


Fig. 5 GNR-TFET operation regimes. The measured experimental data for a fixed back-gate voltage is explained with energy-band diagrams. As side-gate 1 is on the source side and is negatively biased, it makes the GNR source p -type, setting the polarity of the GNR p - n junction. When the drain voltage is large and negative, the p - n diode is forward biased and the normal diode thermionic on-current flows. For small forward biases for smaller negative drain voltages, interband Esaki tunneling current flows from the n -conduction band states to the p -valence-band states, leading to NDR. For positive drain voltages, the GNR is reverse biased and interband Zener tunneling current flows in the device

Figure 4a shows the measured output characteristics of the GNR-TFET measured at room temperature with the two side gates oppositely biased at ± 2.0 V, for various back-gate voltage and drain voltages. A clear and reproducible negative-differential resistance (NDR) is observed at room temperature for a range of back-gate voltages and for negative drain bias voltages. The NDR vanishes for positive drain voltages. If the opposite polarity side-gate voltages are removed, the NDR also vanishes for negative drain voltages, as shown in Fig. 4b. The measured room-temperature characteristics of Fig. 4b are that of a p -channel GNR-FET with no tunneling, whereas that in Fig. 4a is that of a GNR-TFET. This is the report of NDR in a GNR-TFET. The same analytical model that was used for the transfer characteristics in Fig. 3b also qualitatively reproduces the GNR-TFET output characteristics as shown in Fig. 4c. The fact that the model is able to reproduce all essential features of the device attests to its qualitative accuracy. However, the extreme quantized nature of the GNR electronic states implies that the measured experimental data be compared with an atomistic simulation for quantitative insight.

Before setting up the atomistic model, in Fig. 5 we have explained the measured operation regimes of the GNR-TFET through energy-band diagrams. The NDR due to Esaki tunneling should be observed only for negative drain voltages, because the source-end of the GNR is doped p -type by side-gate 1. Under these conditions, the GNR pn junction is under a small forward bias, the regime for interband Esaki tunneling of electrons from the conduction band in the n -side to the empty valence-band states in the p -side. The NDR occurs at the drain bias when the band edges go out of alignment. For positive drain voltages, no NDR is expected, because the current is due to interband Zener tunneling, for which there is no chance for band edges to go out of alignment as indicated in Fig. 5. In Fig. 4a, it is also observed that for positive drain voltages the current monotonically increases and does not turn off. The on/off switching in Fig. 4b, although modest, is much more pronounced when the side gates are not biased. This is because to switch the device off, the back gate must stretch the junction tunneling distance and lower the tunneling probability. However, it is unable to do so because the far stronger electrostatic doping of the two side gates boosted by the polymer electrolyte overrides this desired back-gate control. Thus,

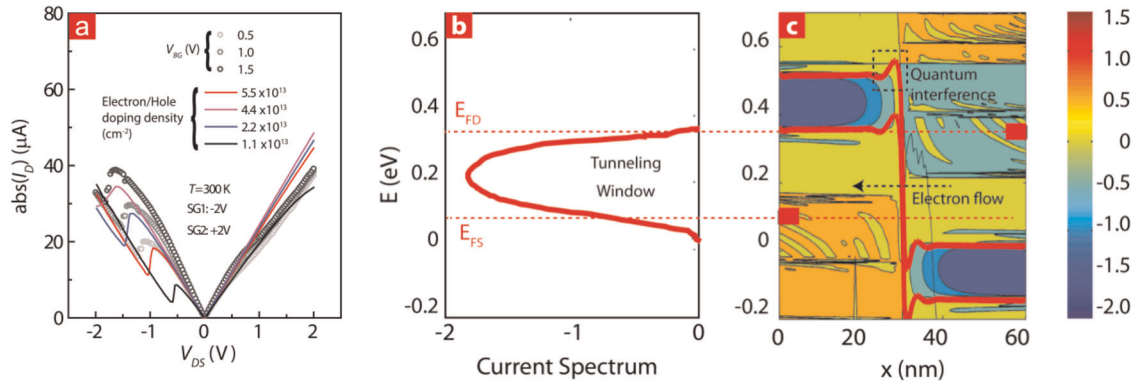


Fig. 6 Numerical atomic simulations of GNR-TFETs. **a** Experimentally measured room-temperature GNR-TFET $I_d - V_{ds}$ characteristics (circles) compared with the numerical atomistic simulation (solid lines). **b** The simulated current spectrum of doping density of $1.1 \times 10^{13}/\text{cm}^2$ at the NDR peak, which is calculated from the transmission multiplied by $(f_S - f_D)$, where f_S and f_D are the Fermi functions of the source and the drain contacts. The current mainly flows in the tunneling window between the source and the drain Fermi level. The minus sign of the current spectrum is because the direction of the current is opposite to that of the x axis, whereby the current in **a** shows only absolute values. **c** The local density of states shown as a contour plot in a logarithmic scale indicated by the color bar. The conduction and valence-band edges are shown in red solid lines. The source and drain Fermi levels (E_{FS}/E_{FD}) are also shown with red dotted lines

although the polymer electrolyte is useful for demonstrating the NDR action, the monotonic increase of the drain current under Zener tunneling also exposes its limitation. To achieve gain in a GNR-TFET, it is desirable that the Zener current saturates and is controlled by the (back) gate voltage as indicated by the gray lines in Fig. 5. These observations point towards the need of direct donor and acceptor doping in the GNR channel without polymer electrolytes in future embodiments, and also underlines the need for narrower GNRs with increased bandgaps in the future. To solidify this qualitative observation, we have employed a comprehensive electrostatic and quantum transport simulation.

The numerical atomistic simulation of the GNR-TFET characteristics is performed using a self-consistent solution of Poisson equation for electrostatics and Schrodinger equation for the electronic bandstructure and quantum transport. For the quantum mechanical portion of the atomistic simulation a p - d tight-binding basis set was used⁴⁵ for determining the energy bandstructure and the transmission formalism was used for calculating the current. Scattering effects are not explicitly included, but lumped into an effective mean-free path and contact resistances (Supplementary Figs S4 and S5). Figure 6a shows the results of the atomistic simulation of the GNR-TFET output characteristics superposed on the measured experimental data. The agreement supports the qualitative analysis and the analytical models, and also offers quantitative insight. For example, the shift in the NDR peak with increasing side-gate doping occurs as the tunneling energy window indicated in Fig. 6b is widened. The energy-resolved current spectrum indicates the peak current flows near the middle of the tunneling window. Although this feature is similar to the increase in Esaki tunneling current as a pn diode is doped heavier, the energy-resolved local density of states (LDOS) in Fig. 6c shows a very abrupt tunnel junction with reflections and interference of electron waves occurring over ~ 4 nm as visible in the LDOS oscillations. Such features are not captured easily in a typical effective mass Wentzel-Kramers-Brillouin (WKB) approximation. The agreement between the experimental data and the numerical model in Fig. 6a also highlights the importance of the atomistic modeling. The performance will continue to improve as the side gate is brought closer to the GNR, while preventing leakage. In addition, the performance will continue to improve if the width is scaled down from the ~ 10 nm to ~ 5 nm, but it will start degrading if the GNR width is scaled down even lower. This is because the I_{off} decreases when the GNR is scaled to smaller widths exponentially as $\sim 1/W$, but the interband tunneling on-current I_{on} decreases with the GNR width exponentially.

To conclude, we have experimentally demonstrated room-temperature operation of atomically thin GNR TFETs. Every feature in the operating characteristics can be understood from a combination of lithographically defined bandgaps and gated interband Esaki and Zener tunneling current flow. The measured NDR tunneling current density is ~ 1 mA/ μm shown in Fig. 4. The larger-than-intended drain voltages necessary are significantly limited by contact and access resistances, as discussed in the Supplementary Materials. The on/off ratio is limited by both the contacts and the wide GNR width. The measured switching performance of these GNR TFETs at this stage are a far cry from what may be considered attractive for realistic applications; scaling of the GNR width and lower contact resistances are predicted to take the GNR-TFET performance close to those predicted in refs.^{27,28} However, the observation of room-temperature gate-tunable NDR in GNR channels is remarkable in its own right. In addition to proving the concept of atomically thin 1D TFETs based on GNRs, the shortcomings of the device reported here also clearly lay down the challenges ahead. Indeed, the control of narrow GNR widths on hBN with controlled edges and orientations, although challenging, was recently reported,^{46,47} which would be beneficial to exploit the inherent advantages of GNRs. The single most challenging task at this juncture to which no clear solution is in sight is to dope the GNR by taking advantage of the broken bonds at the edges. This step would mark a significant breakthrough, because it will not only enable completely controlled GNR TFETs, but also the simpler GNR-FETs – the ideal nanoscale transistors that carbon nanotubes have promised all along.

METHODS

Device fabrication

The GNRs were fabricated by electron-beam lithography (EBL). Hydrogen silsesquioxane (HSQ) diluted with methylisobutylketone is used as a negative electron-beam resist to pattern the GNRs and the details of the entire EBL process have been discussed in previous publications.^{33,48} Figure S1a shows the width of patterned HSQ lines as a function of the electron-beam dose. The width from the scanning electron microscope image in Fig. S1b is proportional to the line dose of the electron beam. After etching away the uncovered graphene by O_2 plasma, the GNR width remains sub-10 nm, showing that the HSQ width is successfully transferred onto the graphene layer. Cr (5 nm)/Au (150 nm) were deposited by e-beam evaporation to form source/drain (S/D), side-gate, and back-gate metal electrodes. The S/D metals sit on top of the zero-bandgap 2D graphene regions to decrease the contact resistance.

Electrostatic doping of GNRs

Unless otherwise stated, all materials were obtained from Sigma Aldrich. One gram of PEO (M_w 100,000 g/mol) was dissolved in 38 g of acetonitrile by mixing with a Teflon stir bar in a Teflon beaker. As commercial PEO contains micrometer-sized particles of SiO_2 , the solution is purified by centrifugation. To purify, the solution is transferred to two 50 mL centrifuge tubes (VWR) and centrifuged at $19,000 \times g$ for 5 min. The transparent supernatant is returned to the Teflon beaker, whereas the precipitate is discarded. Battery-grade LiClO_4 (0.12 g; 99.99% purity) is added to the PEO/acetonitrile solution and stirred for several hours. This PEO: LiClO_4 ratio corresponds to an ether oxygen to Li ratio of 20:1. The solution is spin-coated onto the GNR-TFET at a spin-speed of 1000 RPM for 30 s and annealed for 5 min at 95 °C. This anneal temperature is well above the melting temperature (60 °C) of the polymer electrolyte at an ether oxygen to lithium ratio of 20:1.⁴⁹ The sample is cooled to room temperature by removing it from the hotplate and placing it directly on a cleanroom wipe on the counter top. The thickness of the $(\text{PEO})_{20}:\text{LiClO}_4$ film is 100 nm, measured by ellipsometry. The side-gate metal and the electrolyte act as electrostatic doping agents by manipulating the electric potential of GNRs through mobile Li^+ and ClO_4^- ions in PEO, thus creating a p - n junction.

Analytical model approach

We have used a simple drift-diffusion analytical model to capture the correct electrostatics of the problem (Supplementary Fig. S4), before applying a full quantum transport + electrostatics to explain the experimentally measured device characteristics. The current is the integral of the charge and mobility over the entire channel length. The charge density at a specific location is calculated based on the channel potential and density of states of graphene. The channel potential is solved based on the charge-neutrality equation.

Atomic non-equilibrium Green's function approach

The experimental data were also correlated with an atomistic non-equilibrium Green's function approach based on a p/d orbital tight-binding (p/d TB) model⁵⁰ in which $\{p_z, d_{yz}, d_{zx}\}$ orbitals are included (Supplementary Fig. S5). Although there have been several theoretical studies about GNR TFETs, most of them are limited to the simple p_z orbital tight-binding (p_z TB) model^{51,52} in which only the p_z orbital is included in calculations and some of them are limited to the WKB approximations.²⁸ The simple p_z TB model only works for 2D graphene without considering edge effects. The p/d TB model, however, is more accurate than the simple p_z TB model in terms of the bandstructure, as it is calibrated to first-principle calculations and explicitly includes passivated hydrogen atoms in the Hamiltonian matrix.⁵⁰

DATA AVAILABILITY

All data derived from the experiments and calculations of this study are available from the corresponding author upon reasonable request.

Received: 6 September 2017; Accepted: 16 October 2019;

Published online: 07 November 2019

REFERENCES

- Novoselov, K. S. et al. Electric field effect in atomically thin carbon films. *Science* **306**, 666–669, <https://doi.org/10.1126/science.1102896> (2004).
- Geim, A. K. & Novoselov, K. S. The rise of graphene. *Nat. Mater.* **6**, 183–191, https://doi.org/10.1142/9789814287005_0002 (2007).
- Zhang, Y., Tan, Y.-W., Stormer, H. L. & Kim, P. Experimental observation of the quantum Hall effect and Berry's phase in graphene. *Nature* **438**, 201–204, <https://doi.org/10.1038/nature04235> (2005).
- Jena, D. Tunneling transistors based on graphene and 2-D crystals. *Proc. IEEE* **101**, 1585–1602, <https://doi.org/10.1109/JPROC.2013.2253435> (2013).
- Zhao, P., Feenstra, R. M., Gu, G. & Jena, D. SymFET: a proposed symmetric graphene tunneling field-effect transistor. *IEEE T. Electron. Dev.* **60**, 951–957, <https://doi.org/10.1109/TED.2013.2238238> (2013).
- Mishchenko, A. et al. Twist-controlled resonant tunneling in graphene/boron nitride/graphene heterostructures. *Nat. Nanotechnol.* **9**, 808–813, <https://doi.org/10.1038/nnano.2014.187> (2014).
- Nagashima, A., Tejima, N., Gamou, Y., Kawai, T. & Oshirna, C. Electronic structure of monolayer hexagonal boron nitride physisorbed on metal surfaces. *Phys. Rev. Lett.* **75**, 3918–3921, <https://doi.org/10.1103/PhysRevLett.75.3918> (1995).
- Watanabe, K., Taniguchi, T. & Kanda, H. Direct-bandgap properties and evidence for ultraviolet lasing of hexagonal boron nitride single crystal. *Nat. Mater.* **3**, 404–409, <https://doi.org/10.1038/nmat1134> (2004).
- Dean, C. R. et al. Boron nitride substrate for high-quality graphene electronics. *Nat. Nanotechnol.* **5**, 722–726, <https://doi.org/10.1038/nnano.2010.172> (2010).
- Meric, I. et al. Graphene field-effect transistors based on boron-nitride dielectrics. *Proc. IEEE* **101**, 1609–1619, <https://doi.org/10.1109/JPROC.2013.2257634> (2013).
- Jang, S. K., Youn, J., Song, Y. J. & Lee, S. Synthesis and characterization of hexagonal boron nitride as a gate dielectric. *Sci. Rep.* **6**, 30449, <https://doi.org/10.1038/srep30449> (2016).
- Radisavljevic, B., Radenovic, A., Brivio, J., Giacometti, V. & Kis, A. Single-layer MoS_2 transistors. *Nat. Nanotechnol.* **6**, 147–150, <https://doi.org/10.1021/nn2024557> (2011).
- Kim, S. et al. High-mobility and low-power thin-film transistors based on multi-layer MoS_2 crystals. *Nat. Commun.* **3**, 1011, <https://doi.org/10.1038/ncomms2018> (2012).
- Li, X. et al. Controlled vapor phase growth of single crystalline, two-dimensional GaSe crystals with high photoresponse. *Sci. Rep.* **4**, 5497, <https://doi.org/10.1038/srep05497> (2014).
- Ohta, T., Bostwick, A., Seyller, T., Horn, K. & Rotenberg, E. Controlling the electronic structure of bilayer graphene. *Science* **313**, 951–954, <https://doi.org/10.1126/science.1130681> (2006).
- Zhang, Y. et al. Direct observation of a widely tunable bandgap in bilayer graphene. *Nature* **459**, 820–823, <https://doi.org/10.1038/nature08105> (2009).
- Rudenko, A. N. & Katsnelson, M. I. Quasiparticle band structure and tight-binding model for single- and bilayer black phosphorus. *Phys. Rev. B* **89**, 201408(R), <https://doi.org/10.1103/PhysRevB.89.201408> (2014).
- Lu, J. et al. Bandgap engineering of phosphorene by laser oxidation toward functional 2D materials. *ACS Nano* **9**, 10411–10421, <https://doi.org/10.1021/acsnano.5b04623> (2015).
- Charlier, J.-C., Blas, X. & Roche, S. Electronic and transport properties of nanotubes. *Rev. Mod. Phys.* **79**, 677–732, <https://doi.org/10.1103/RevModPhys.79.677> (2007).
- Franklin, A. D. et al. Sub-10 nm carbon nanotube transistor. *Nano Lett.* **12**, 758–762, <https://doi.org/10.1021/nl203701g> (2012).
- Arnold, M. S., Green, A. A., Hulvat, J. F., Stupp, S. I. & Hersam, M. C. Sorting carbon nanotubes by electronic structure using density differentiation. *Nature* **1**, 60–65, <https://doi.org/10.1038/nnano.2006.52> (2006).
- Wang, C. et al. Wafer-scale fabrication of separated carbon nanotube thin-film transistors for display applications. *Nano Lett.* **9**, 4285–4291, <https://doi.org/10.1021/nl902522f> (2009).
- Appenzeller, J., Lin, Y.-M., Knoch, J. & Avouris, Ph Band-to-band tunneling in carbon nanotube field-effect transistors. *Phys. Rev. Lett.* **93**, 196805, <https://doi.org/10.1103/PhysRevLett.93.196805> (2004).
- Ionescu, A. M. & Riel, H. Tunnel field-effect transistors as energy efficient electronic switches. *Nature* **479**, 329–337, <https://doi.org/10.1038/nature10679> (2011).
- Ma, N. & Jena, D. Interband tunneling in two-dimensional crystal semiconductors. *Appl. Phys. Lett.* **102**, 132102, <https://doi.org/10.1063/1.4799498> (2013).
- Jena, D., Fang, T., Zhang, Q. & Xing, H. Zener tunneling in semiconducting nanotube and graphene nanoribbon p - n junctions. *Appl. Phys. Lett.* **93**, 112106, <https://doi.org/10.1063/1.2983744> (2008).
- Nikonov, D. E. & Young, I. A. Benchmarking of beyond-CMOS exploratory devices for logic integrated circuits. *IEEE J. Explor. Solid State Computat. Devices Circuits* **1**, 1–11, <https://doi.org/10.1109/JXCDC.2015.2418033> (2015).
- Zhang, Q., Fang, T., Xing, H., Seabaugh, A. & Jena, D. Graphene nanoribbon tunnel transistors. *IEEE Electr. Device Lett.* **29**, 1344–1346, <https://doi.org/10.1109/LED.2008.2005650> (2008).
- Han, M. Y., Özyilmaz, B., Zhang, Y. & Kim, P. Energy band-gap engineering of graphene nanoribbons. *Phys. Rev. Lett.* **98**, 206805, <https://doi.org/10.1103/PhysRevLett.98.206805> (2007).
- Li, X. et al. Large-area synthesis of high-quality and uniform graphene films on copper foils. *Science* **324**, 1312, <https://doi.org/10.1126/science.1171245> (2009).
- Liao, A. D. et al. Thermally limited current carrying ability of graphene nanoribbons. *Phys. Rev. Lett.* **106**, 256801, <https://doi.org/10.1103/PhysRevLett.106.256801> (2011).
- Hwang, W. S. et al. Graphene nanoribbon field-effect transistors on wafer-scale epitaxial graphene on SiC substrates. *APL Mater.* **3**, 011101, <https://doi.org/10.1063/1.4905155> (2015).
- Hwang, W. S. et al. Transport properties of graphene nanoribbon transistors on chemical-vapor-deposition grown wafer-scale graphene. *Appl. Phys. Lett.* **100**, 203107, <https://doi.org/10.1063/1.4716983> (2012).

34. Nilsson, H. A. et al. Temperature dependent properties of InSb and InAs nanowire field-effect transistors. *Appl. Phys. Lett.* **96**, 153505, <https://doi.org/10.1063/1.3402760> (2010).
35. Lee, H. et al. Sub-5 nm all-around gate FinFET for ultimate scaling. *2006 Symposium on VLSI Technology. Digest of Technical Papers.* 58–59, <https://doi.org/10.1109/VLSIT.2006.1705215> (2006).
36. Williams, J. R., DiCarlo, L. & Marcus, C. M. Quantum Hall effect in a gate-controlled *p-n* junction of graphene. *Science* **317**, 638, <https://doi.org/10.1126/science.1144657> (2007).
37. Farmer, D. B., Lin, Y. –M., Afzali-Ardakani, A. & Avouris, P. Behavior of a chemically doped graphene junction. *Appl. Phys. Lett.* **94**, 213106, <https://doi.org/10.1063/1.3142865> (2009).
38. Huard, B., Stander, N., Sulpizio, J. A. & Goldhaber-Gordon, D. Evidence of the role of contacts on the observed electron-hole asymmetry in graphene. *Phys. Rev. B* **78**, 121401(R), <https://doi.org/10.1103/PhysRevB.78.121402> (2008).
39. Romero, H. E. et al. N-type behavior of graphene supported on Si/SiO₂ substrates. *ACS Nano* **2**, 2037–2044, <https://doi.org/10.1021/nn800354m> (2008).
40. Wang, X. et al. N-doping of graphene through electrothermal reactions with ammonia. *Science* **324**, 768–771, <https://doi.org/10.1126/science.1170335> (2009).
41. Ueno, K. et al. Electric-field-induced superconductivity in an insulator. *Nat. Mater.* **7**, 855, <https://doi.org/10.1038/nmat2298> (2008).
42. Welton, T. Room-temperature ionic liquids. Solvents for synthesis and catalysis. *Chem. Rev.* **99**, 2071, <https://doi.org/10.1021/cr980032t> (1999).
43. Ye, Y.-S. et al. Ionic liquid polymer electrolytes. *J. Mater. Chem. A* **1**, 2719, <https://doi.org/10.1039/C2TA00126H> (2013).
44. Efetov, D. K. & Kim, P. Controlling electron-phonon interactions in graphene at ultrahigh carrier densities. *Phys. Rev. Lett.* **105**, 256805, <https://doi.org/10.1103/PhysRevLett.105.256805> (2010).
45. Luisier, M. & Klimeck, G. Performance analysis of statistical samples of graphene nanoribbon tunneling transistors with line edge roughness. *Appl. Phys. Lett.* **94**, 223505, <https://doi.org/10.1063/1.3140505> (2009).
46. Chen, L. et al. Oriented graphene nanoribbons embedded in hexagonal boron nitride trenches. *Nat. Commun.* **8**, 14703, <https://doi.org/10.1038/ncomms14703> (2017).
47. Che, L. et al. Edge control of graphene domains grown on hexagonal boron nitride. *Nanoscale* **9**, 11475, <https://doi.org/10.1039/C7NR02578E> (2017).
48. Hwang, W. S. et al. Fabrication of top-gated epitaxial graphene nanoribbon FETs using hydrogen-silsesquioxane. *J. Val. Sci. Technol.* **B 30**, 03D104, <https://doi.org/10.1116/1.3693593> (2012).
49. Robitaille, C. & Fauteux, D. Phase-diagrams and conductivity characterization of some PEO-Lix electrolytes. *J. Elec. Soc.* **133**, 315, <https://doi.org/10.1149/1.2108569> (1986).
50. Boykin, T. B. et al. Accurate six-band nearest-neighbor tight-binding model for the π -bands of bulk graphene and graphene nanoribbons. *J. Appl. Phys.* **109**, 104304, <https://doi.org/10.1063/1.3582136> (2011).
51. Luisier, M. & Klimeck, G. Performance analysis of statistical samples of graphene nanoribbon tunneling transistors with line edge roughness. *Appl. Phys. Lett.* **94**, 223505, <https://doi.org/10.1063/1.3140505> (2011).
52. Fiori, G. & Iannaccone, G. Simulation of graphene nanoribbon field-effect transistors. *IEEE Elec. Dev. Lett.* **28**, 760, <https://doi.org/10.1109/LED.2007.901680> (2007).

ACKNOWLEDGEMENTS

This research made use of the Cornell Nanofabrication Facility and the Center for Nano Science and Technology at University of Notre Dame, which were supported in part by the Semiconductor Research Corporation (SRC), Nanoelectronics Research

Initiative (NRI), and the National Institute of Standards and Technology (NIST) through the Midwest Institute for Nanoelectronics Discovery (MIND), STARnet, an SRC program sponsored by MARCO and DARPA, and by the Office of Naval Research (ONR) and the National Science Foundation (NSF). The authors acknowledge the single layer graphene provided by Dr Chun-Yung Sung (from the IBM T. J. Watson Center at the time). The authors also acknowledge the nanoHUB.org computing resources provided by the National Institute for Computational Sciences (NICS) and by Network for Computational Nanotechnology funded by the National Science Foundation. W.S.H. is grateful to Center for Advanced Soft Electronics funded by the Ministry of Science, ICT, and Future Planning as Global Frontier Project (CASE-2011-0031638) and Basic Science Research Program (2017R1A2B4012278) by the National Research Foundation of Korea (NRF).

AUTHOR CONTRIBUTIONS

W.S.H., A.S. and D.J. designed the experiment. W.S.H., R.Y. and S.K.F.-S. fabricated and prepared the samples. P.Z., S.G.K., G.K. and D.J. performed the models and simulations. W.S.H., G.K., A.S., S.K.F.-S., H(G).X. and D.J. analysed the data. W.S.H., S. G.K., G.K., S.K.F.-S. and D.J. wrote the manuscript. All authors discussed the data and contributed to the manuscript.

COMPETING INTERESTS

The authors declare no competing interests.

ADDITIONAL INFORMATION

Supplementary information is available for this paper at <https://doi.org/10.1038/s41699-019-0127-1>.

Correspondence and requests for materials should be addressed to W.S.H. or D.J.

Reprints and permission information is available at <http://www.nature.com/reprints>

Publisher's note Springer Nature remains neutral with regard to jurisdictional claims in published maps and institutional affiliations.



Open Access This article is licensed under a Creative Commons Attribution 4.0 International License, which permits use, sharing, adaptation, distribution and reproduction in any medium or format, as long as you give appropriate credit to the original author(s) and the source, provide a link to the Creative Commons license, and indicate if changes were made. The images or other third party material in this article are included in the article's Creative Commons license, unless indicated otherwise in a credit line to the material. If material is not included in the article's Creative Commons license and your intended use is not permitted by statutory regulation or exceeds the permitted use, you will need to obtain permission directly from the copyright holder. To view a copy of this license, visit <http://creativecommons.org/licenses/by/4.0/>.

© The Author(s) 2019

Supplementary Information

Room-Temperature Graphene-Nanoribbon Tunneling Field-Effect Transistors

Wan Sik Hwang^{1,3,5}, Pei Zhao³, Sung Geun Kim⁴, Rusen Yan¹, Gerhard Klimeck⁴, Alan Seabaugh³, Susan K. Fullerton-Shirey^{3,6}, Huili (Grace) Xing^{1,2,3}, and Debdeep Jena^{1,2,3}

¹Dept. of Electrical and Computer Engineering, Cornell University, Ithaca, NY, 14853, USA

²Dept. of Materials Science and Engineering, Cornell University, Ithaca, NY, 14853, USA

³Dept. of Electrical Engineering, University of Notre Dame, Notre Dame, IN, 46556, USA

⁴Dept. of Electrical and Computer Engineering, Purdue University, West Lafayette, IN, 47906, USA

⁵Dept. of Materials Engineering, Korea Aerospace University, Goyang, 10540, Korea

⁶Dept. of Chemical and Petroleum Engineering, University of Pittsburgh, Pittsburgh, PA 15213, USA

Corresponding authors' email addresses: whwang@kau.ac.kr & djena@cornell.edu

1. Supplementary Figures

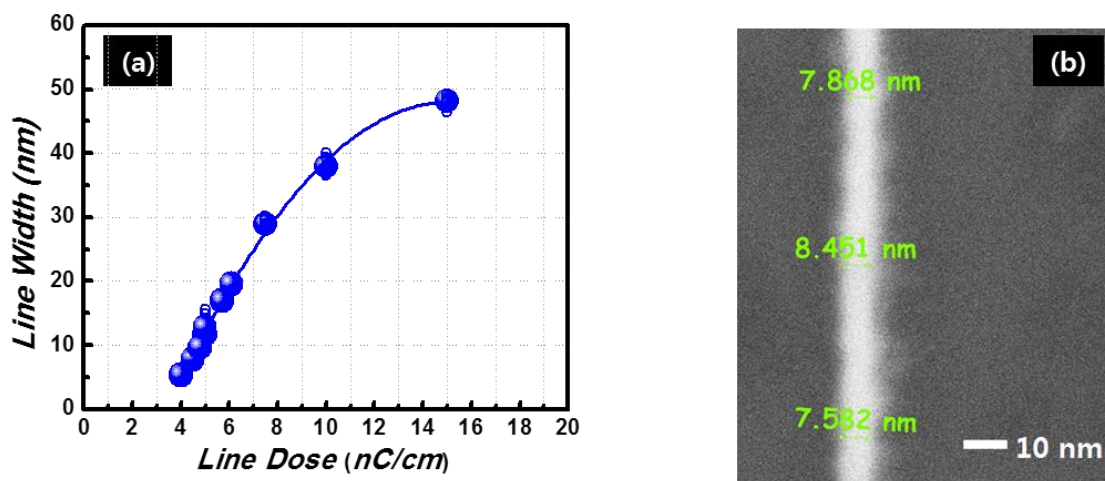


Figure S1. Formation of graphene nano-ribbons (GNRs) and GNR FETs: Hydrogen silsesquioxane was used as the resist for electron-beam lithography to pattern the graphene nanoribbons. **a)** Hydrogen silsesquioxane line-width as a function of the line dose used in the electron beam lithography [1]. **b)** Scanning electron microscope image of the hydrogen silsesquioxane line-width; the hydrogen silsesquioxane pattern observed here is transferred to the graphene after etching, forming graphene nanoribbons of similar widths as the pattern.

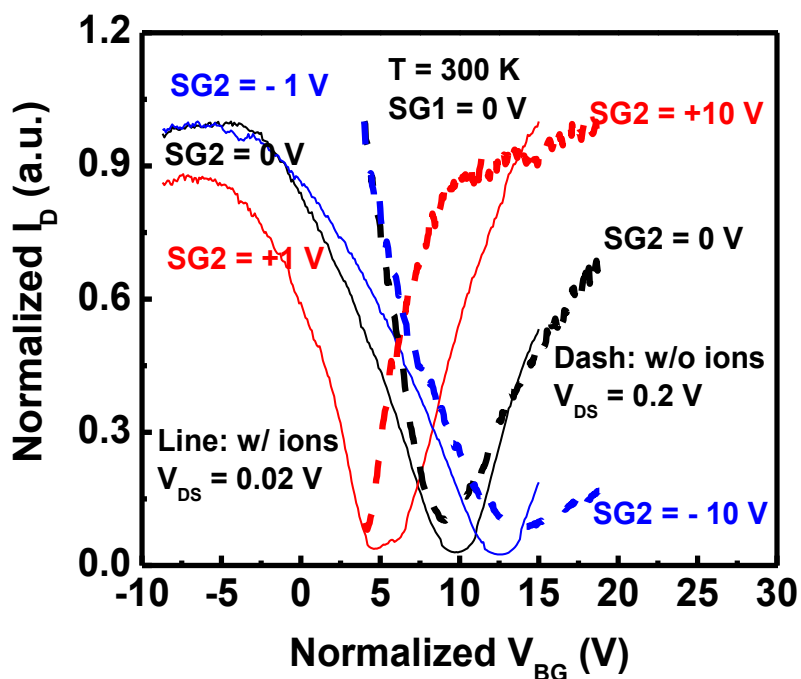


Figure S2. Electrostatic doping of GNRs using the solid polymer electrolyte, PEO:LiClO₄: Normalized drain current flowing through the graphene nanoribbon as a function of normalized back-gate voltage with ion-assisted (solid lines) and without ion-assisted (dashed lines) electrostatic doping. The shift in the charge neutrality point due to electrostatic doping with the solid polymer electrolyte in solid lines needs only +/- 1 Volt to achieve what requires more than +/- 10 Volts on the side gates when performed without the electrolyte gating.

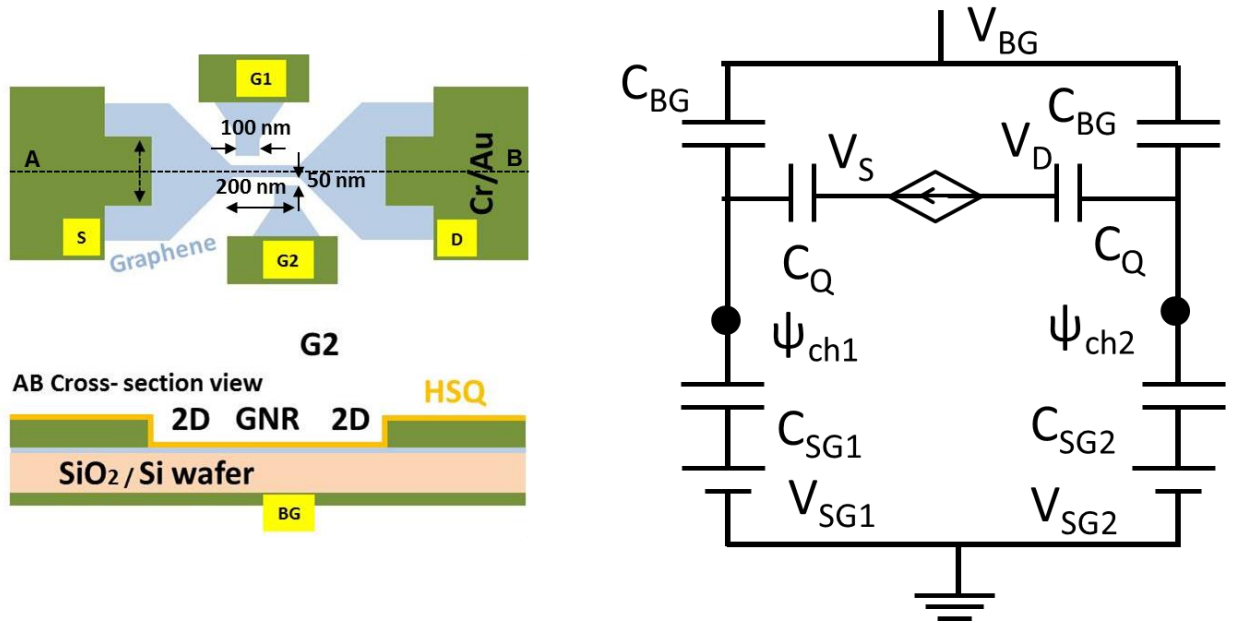


Figure S3. Graphene nanoribbon tunnel-field effect transistor device geometry top and side views, and the corresponding simple circuit model that is used for analytical modeling.

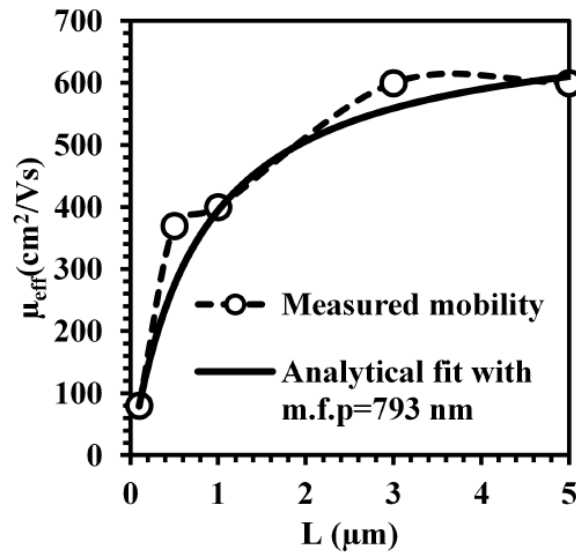


Figure S4. Effective mobility μ_{eff} as a function of the channel length L is obtained from the experimentally measured the I_D - V_D characteristics through fitting [9] to an analytical formula [10]. The effective mobility calculated from an analytical relation between long channel mobility to the short channel mobility is fitted to the previously calculated effective mobility with a least square fit. The mean free path λ of 793 nm and long channel mobility of 707 cm²/Vs give the best fit.

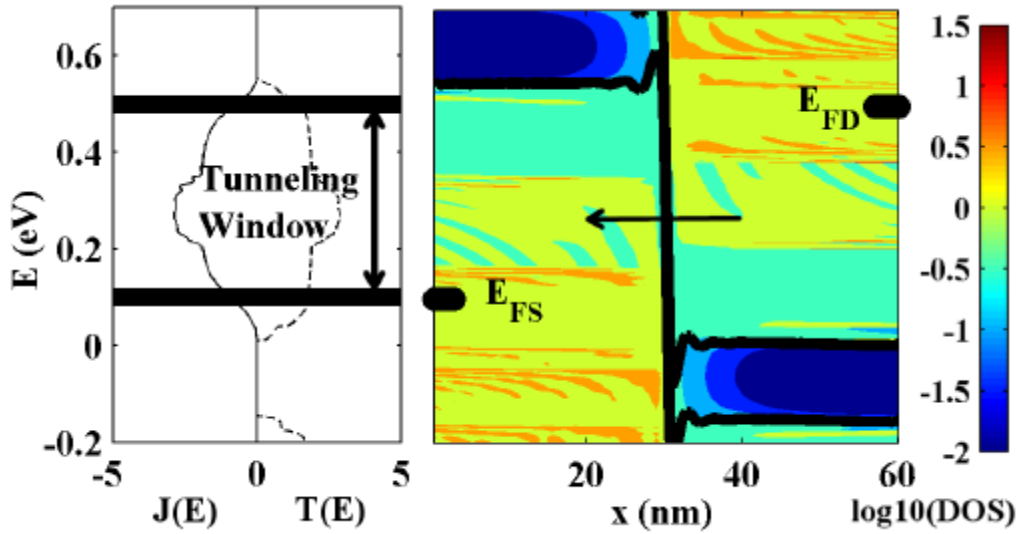


Figure S5. Current spectrum and density of state for the doping of $2.2 \times 10^{13} / \text{cm}^2$.

2. Supplementary Methods

Figure S2 shows normalized I_D as a function of normalized V_{BG} at with ion-assisted and without ion-assisted electrostatic doping. It shows that side gates (without ions) can modulate the charge carrier density in the GNR channel, but needing much higher side gate voltages compared to the side gates with ions. It also shows that ions in the polymer minimize the parasitic capacitance and can enhance the GNR channel controllability to form an abrupt pn Esaki junction in the GNR.

3. Supplementary Discussion

Analytical modeling of the GNR device characteristics : Figure S3 shows the top and side view of the GNR TFET structure, and a simple circuit model for the device accounting for the various capacitive couplings. The circuit gives the charge neutrality condition in the transistor where ψ_{ch1} and ψ_{ch2} are the channel potentials under the control of side gate1, side gate2 and the back gate, and C_q is the density-of-states or quantum capacitance of the graphene nanoribbon channel.

The current is calculated by the the Shockley gradual channel drift-diffusion model

$$I = q \frac{W}{L} \int_0^L n(x) v_{drift}(x) dx, \quad (1)$$

where q is the electron charge, W and L are the width and length of the GNR, $n(x)$ the carrier density in the channel at x , the coordinate from the source to drain. The drift velocity of carriers is

$$v_{drift} = \frac{\mu F}{1 + \mu F / v_{sat}}, \quad (2)$$

where m is the electron mobility, v_{sat} the saturation velocity, and F is the electric field in the x -direction. The carrier density is related to the local channel potential, the bandgap by

$$n(x) = \int D(E - \varphi_{ch}(x) - \frac{E_G}{2}) \cdot f(E - \mu(x)) dE, \quad (3)$$

where $D(E - \varphi_{ch}(x) - E_G/2)$ is the density-of-states of the GNR, and $f(x)=1/(1+\exp[x])$ is the Fermi-Dirac function. The channel potential is obtained by solving the charge neutrality equation based on the circuit model shown in Fig S3:

$$\left(\frac{\varphi_{ch}(x)}{q} + V_{BG}(x) \right) \cdot C_{BG} + \left(\frac{\varphi_{ch}(x)}{q} + V_{SG}(x) \right) \cdot C_{SG1,2} + \left(\frac{\varphi_{ch}(x)}{q} - \frac{\mu(x)}{q} \right) \cdot \frac{C_q}{2} + qn_0 = 0, \quad (4)$$

where n_0 is the background impurity density, C_{BG} and C_{SG} are the back gate and side gate capacitances. Based on the model above, with an effective oxide thickness $EOT_{SG} = 1$ nm and $EOT_{SG} = 4.5$ nm was used to plot the transfer curves shown in Figs. 3(b). The good agreement with the measured values in Fig 3(a) suggest the above model captures the electrostatics accurately. Using this electrostatics model, we added a simple analytical WKB component to the current to further capture the NDR as indicated in Fig 4(c), under the appropriate bias conditions to compare to the experimental measurement in Fig 4(a). Even though the calculated current is much larger

than experimental results due to the lack of the additional contact resistance in the simple model, the $I_{PEAK} - I_{valley}$ in the NDR region is very close, and the model also captures the correct polarity for the Esaki NDR tunneling in the $-ve$ bias, and the Zener interband tunneling in the forward bias condition. For higher precision, a numerical simulation combining electrostatics with quantum transport is next described.

Atomic Non-equilibrium Green's function approach: The simulated structure is a $p-n$ diode with the length of the p - and n -type regions equal to 30 nm. The effective doping density is assumed to reflect electrostatic doping. Since the simulation is conducted in a ballistic regime, a more realistic comparison with experimental data requires taking into account scattering. The ratio between the ballistic current and the scattering limited current is calculated from [1].

$$\frac{I_{scatt}}{I_{ball}} = \frac{T}{2-T}, T = \frac{\lambda}{L+\lambda}, \quad (5)$$

This equation requires the mean free path for scattering, λ , to calculate the scattering limited current. The mean free path for scattering is calculated from the effective mobility μ_{eff} extracted from the measured I_D-V_D characteristics of the GNR-FET structure. The measured I_D-V_D characteristics are fitted with the analytical model [2], allowing μ_{eff} only as a fitting parameter [3]. The mean free path is then obtained by fitting the μ_{eff} vs. channel length curve to the experimental data. For a given λ , the μ_{eff} can be calculated from the relationship between the long channel mobility μ_{long} and μ_{eff} [1]:

$$\frac{\mu_{eff}}{\mu_{long}} = \frac{L}{L+\lambda}, \quad (6)$$

A mean free path = 793 nm and $\mu_{long} = 707 \text{ cm}^2/\text{Vs}$ give the best fit to the measured data using least square method as shown in Fig. S4. After the ballistic current is calculated from

quantum transport calculations, the scattering limited current is calculated from Eq. 1 using $\lambda = 793$ nm. It is noted that the results in the fig. S4 was extracted from epi-graphene but the scattering caused by GNR edge should be comparable to that from CVD graphene since the entire process integration including GNR formation is identical both of them. Then the series resistance R_{SD} is tuned to match the simulated thermionic current part with experimental data. The resulting R_{SD} is 300 Ω m. The trend and the shape of the calculated I_D - V_D matches well the experimental data. However, the simulation data are for a symmetrically doped un-gated p - n diode while the experimental data are for a tunneling transistor with a p - n junction and a back-gate. Therefore, the results need some interpretations. The experimental I_D - V_D characteristics show no NDR at $V_G = 0$ V. This indicates that when no back-gate voltage is applied, the effective doping concentration of either p - or n -doped region is not big enough to allow (Esaki) tunneling to occur. This can be explained by the following. Without a voltage applied to the side gates, the original GNR is a strong p -type. With a side-gate voltage $V_{G1} = -2$ V, the GNR under the side-gate G1 becomes a weak n -type while a side-gate voltage $V_{G2} = 2$ V gives an even stronger p -type for the GNR under the side-gate G2. This implies that, without a back-gate voltage, the p - n junction doping concentration is asymmetric ($p+++n-$). Only when a back-gate voltage is applied, the overall bands are shifted down (because the back-gate covers the whole region of the GNR) and the effective doping concentration of the n -doped region starts to be comparable to that of p -doped region and hence the I_D - V_D characteristic shows a strong NDR. When the NDR peak becomes the largest, the p - n doping is the closest to symmetric. Therefore, the effective doping concentrations in the experimental structure can be estimated by comparing the tunneling current at the maximum NDR peak of the experimental data to the NDR peak of the simulation data. Since the NDR peak in the simulation data with $N_S = N_D = 5.5 \times 10^{13}$ cm^{-2} is similar to the maximum NDR peak current

in the experimental data at $V_G=1.5$ V, the effective doping concentrations of the p - and n -doped regions created experimentally are estimated to be $5.5 \times 10^{13} \text{ cm}^{-2}$.

Notice that not only the peak is similar, but the overall shape including the drain voltage V_D where the NDR occurs is also very similar. Both the tunneling current and the drain voltage at the NDR peak are determined by tunneling window $E_{FD} - E_{FS}$ where E_{FS}/E_{FD} is the source/drain Fermi level as shown in Fig. S5. Therefore, the tunneling window for different back-gate bias V_G in experiment can be estimated from the simulation results as well. These results as a whole confirm a successful creation of a GNR tunneling transistor with a capability of the back-gate controlling the tunneling current magnitude. Optimizing the GNR TFET structure is beyond the scope of this article, but one can argue that doping modulation in TFETs can drastically change their on/off current [4]

4. Supplementary References

[1] Jeong, C., Antoniadis, D. A. & Lundstrom, M. S. On backscattering and mobility in nanoscale silicon MOSFETs, *IEEE Trans. Elec. Dev.* **56**, 2762 [10.1109/TED.2009.2030844](https://doi.org/10.1109/TED.2009.2030844) (2009).

[2] Meric, I. et al. Current saturation in zero-bandgap, top-gated graphene field-effect transistors, *Nature Nanotech.* **3**, 654 <https://doi.org/10.1038/nnano.2008.268> (2008)

[3] Hwang, W. S. et al. Electronic transport properties of top-gated epitaxial-graphene nanoribbons field-effect transistors on SiC wafers. *J. of Vac. Sci. Tech. B* **32**, 012202 <https://doi.org/10.1116/1.4861379> (2014)

[4] Knoch, J. Optimizing tunnel FET performance – Impact of device structure, transistors dimensions and choice of material, *VLSI Tech., System and application, Int. Symp.* 45 [10.1109/VTSA.2009.5159285](https://doi.org/10.1109/VTSA.2009.5159285) (2009).